

1 **Fully-resolved simulations of single char**
2 **particle combustion using a ghost-cell**
3 **immersed boundary method**

4 By

5 Kun Luo¹, Chaoli Mao¹, Nils Erland L. Haugen^{2,3}, Jianren Fan^{1,*}, Zhenya
6 Zhuang¹

7 1 State Key Laboratory of Clean Energy Utilization, Zhejiang University, Hangzhou
8 310027, P.R. China

9 2 SINTEF Energy Research, N-7465 Trondheim, Norway

10 3 Department of Energy and Process Engineering, Norwegian University of Science
11 and Technology Kolbjørn Hejes vei 1B, NO-7491 Trondheim, Norway

12

13

14

15

16

17

18

19

20

Submitted to

21

AIChE Journal

22

23 **Abstract**

24 A novel ghost-cell immersed boundary method for fully resolved simulation of
25 char particle combustion has been developed. The boundary conditions at the solid
26 particle surface, such as velocity, temperature, density and chemical species
27 concentration, are well enforced through the present method. Two semi-global
28 heterogeneous reactions and one homogeneous reaction are used to describe the
29 chemical reactions in the domain, and the Stefan flow caused by the heterogeneous
30 reactions is considered. A satisfactory agreement can be found between the present
31 simulation results and experimental data in the literature. The method is then used to
32 investigate the combustion property of a char particle and the interaction between CO₂
33 gasification and O₂ oxidation. Furthermore, combustion effect on the exchange of mass,
34 momentum and energy between gas- and solid- phase is explored.

35

36 **Keywords:** Immersed boundary method; ghost-cell; char combustion; fully resolved
37 simulation

38

39 List of Figure Captions

40 **Figure 1.** Extrapolation implementation for the present ghost-cell immersed boundary
41 method. (° : ghost points, ° (M): mirror points, ° (1, 2): probe points, ● : boundary
42 intersection (BI) points, □ : fluid points.)

43 **Figure 2.** L_2 -norms computed at different grid levels.

44 **Figure 3.** Schematic of the experiment by Makino et al³⁴.

45 **Figure 4.** Schematic of computational domain.

46 **Figure 5.** Temperature evolution of the graphite rod during combustion.

47 **Figure 6.** Carbon burning rate at different surface temperatures.

48 **Figure 7.** CO flame around the burning carbon surface at different temperatures.

49 **Figure 8.** The dominant surface reaction changing from R1 ($2C-O_2 \rightarrow 2CO$) to R2
50 ($C-CO_2 \rightarrow 2CO$).

51 **Figure 9.** Evolution of averaged char consumption rate versus Reynolds number.

52 **Figure 10.** The averaged concentration of O_2 and CO_2 under different Re_{ps} .

53 **Figure 11.** The influence of Reynolds number on averaged transportation

54 **Figure 12.** Respective contribution of O_2 and CO_2 to the production of CO on the
55 surface.

56 **Figure 13.** Reactive zones of gas-phase in terms of CO consumption rate.

57 **Figure 14.** Distribution of convective and diffusive Da number along x at $y=0$.

58 **Figure 15.** The local consumption or production rate of different species.

59 **Figure 16.** Evolution of C_d , Nu and Sh number with Reynolds number.

60 **Figure 17.** Temperature contour under different Reynolds numbers.

61 **Figure 18.** Schematic of a burning carbon surface

62

63

64

65 **Introduction**

66 Coal is one of the most available mineral resources used as a primary fuel for
67 energy production. However, coal combustion has a serious environmental impact
68 linked with the continuously increased emission of carbon dioxide, sulfur dioxide,
69 nitrogen oxides and fine particles into the atmosphere. In order to improve the design
70 of combustion devices with enhanced combustion efficiency and reduced pollutant
71 emission, it requires a deep understanding of the complex multi-physics and
72 multi-scale interactions coupled in the coal combustion process, as well as an accurate
73 predictive capability of this process. With this background it is clear that, the
74 investigation of the coal combustion process is of vital importance.

75 Char combustion plays an important role in the coal combustion process and a
76 detailed understanding of the underlying physical phenomena in the char combustion
77 process is crucial for correct modelling of coal combustion. Typically, point particle
78 models are used for simulation of particulate flow with char combustion in industrial
79 devices. However, errors associated with these simplified char combustion sub-models
80 such as the single-film model proposed by Nusselt¹ and the double-film model², need
81 to be quantified and the constraints within which a given model is feasible should be
82 assessed. Thus, a fully resolved numerical simulation method, in which the solid-gas
83 interface and particle boundary layer are spatially and chemically resolved, is needed
84 to describe the complete char combustion process³. Simulation results based on this
85 method can be used to understand the underlying physical processes and to improve,
86 assess and even develop new accurate models using point particle assumption for
87 large scale simulations. There are basically two approaches to implement the fully
88 resolved simulation, including (1) body-conformal grid methods and (2) fixed-grid
89 methods. Since rapid particle moving/deforming processes are often involved in the

90 char combustion process and the phase-interface changes correspondingly, frequent
91 re-meshing process will be needed in body-conformal grid methods, which will
92 consume tremendous computer resources. Thus, a fixed-grid method will be more
93 desirable in such a simulation.

94 The immersed boundary (IB) method is one of the fixed-grid methods and has
95 been demonstrated to have the capability of handling complex fluid-structure
96 interaction problems with high efficiency. The advantages of the IB method, such as
97 simplicity in grid generation, savings in computer resources and straightforward
98 parallelization, have expanded its applications in multiphase flow simulations.

99 The immersed boundary method was first introduced by Peskin⁴ to simulate the
100 blood flow around a human heart valve. The main idea of this method is to use a
101 Cartesian grid for fluid flow simulation together with a Lagrangian representation of
102 the immersed boundary. A forcing term is introduced to represent the interaction
103 between the immersed boundary and the fluid, and a discrete Dirac-delta function is
104 used to smooth this singular force on the Eulerian grid.⁵ Since then, numerous
105 modifications and improvements have been made, which are well discussed and
106 categorized.⁶⁻⁸ The idea of the ghost cell immersed boundary (GCIB) method is based
107 on the work of Fadlun et al⁹. The GCIB method treats the immersed boundary as a
108 sharp interface, and does not require the explicit addition of discrete forces in the
109 governing equations, thus it can be easily combined with the existing solvers. The
110 boundary condition on the IB is enforced through the “ghost cells”. The variable
111 values of the ghost cells are calculated with the IB boundary conditions and the fluid
112 variables near the boundary. The flow solver senses the presence of the immersed
113 boundary through the extrapolated values at the ghost points.¹⁰ The GCIB method has
114 shown large potential to handle different fluid-solid interaction problems, including

115 those involving highly complex geometries¹¹⁻¹³ and moving/deforming objects¹⁴⁻¹⁶.

116 Extension of the immersed boundary method to heat transfer problems has gained
117 its popularity since Kim and Choi¹⁷. Many researchers have paid their effort to
118 improve the accuracy of immersed boundary methods and broaden its application in
119 heat transfer simulations. In our previous work¹⁸, a ghost-cell compressible IB method
120 of second-order accuracy is designed to enforce Dirichlet, Neumann and Robin type
121 thermal boundary conditions. And an extension to complex phase-interface is made by
122 Luo et al¹⁹. But until now, there are few studies about the immersed boundary method
123 involving multiphase chemical reactions. McGurn et al²⁰ investigated the conjugate
124 heat and mass transfer processes associated with charring solids. The moving
125 interface is described by a level-set method and the boundary condition is enforced
126 through a ghost-fluid methodology. The effects of surface blowing from off-gassing
127 are superimposed through an explicit source term deposition into the Eulerian gas
128 field. Kedia et al²¹ introduced a “buffer zone” methodology to simulate the reacting
129 flow around a solid object. Their method imposes the conjugate boundary condition
130 for heat transfer and non-penetration boundary condition for species concentration on
131 the immersed boundary and is able to track the flame around the object. Deen and
132 Kuipers²² extended the immersed boundary method to simulate infinitely fast
133 heterogeneous reactions happened at the exterior surface of the particles, but the mass
134 source caused by the surface reactions is not considered. **As for other fix-grid methods,**
135 **a new model to a track reacting particle interface and particle porosity has been**
136 **presented very recently²³. Simulation results there showed that the Stefan flow**
137 **significantly modified the mass transfer process governed by the Thiele modulus and**
138 **the hydrodynamic boundary layer around the particle, indicating crucial importance of**
139 **the particle-resolved combustion simulation.** Since the implementation of the

140 immersed boundary for the gas-solid chemical reactions are still rare, it is desirable to
141 develop an efficient IB method for multiphase combustion process.

142 The main objective of the present work is to develop a novel ghost-cell immersed
143 boundary method for char combustion process based on the work of Luo et al¹⁸. The
144 interaction between immersed body and the fluid is expressed by ghost points inside
145 the immersed bodies, and these ghost points ensure that boundary conditions are
146 satisfied precisely on the immersed boundary. Different reconstruction stencils are
147 carried out to enforce the boundary conditions of different variables.

148 The reminder of the present paper is organized as follows. Section 2 and 3
149 describe the numerical methodology including the flow solver and the ghost-cell
150 immersed boundary method for gas-solid chemical reactions. Section 4 describes the
151 problem set-ups and some assumptions. In section 5, the capability of the proposed
152 methodology to handle char combustion process is validated and further investigation
153 is carried out. Section 6 is devoted to discussions and conclusions.

154 **Governing equations**

155 The continuity equation is solved in the form^{24, 25},

$$156 \quad \frac{D\rho}{Dt} + \rho \nabla \cdot \mathbf{u} = 0, \quad (1)$$

157 where ρ is the density, \mathbf{u} is the fluid velocity, t is time and $D/Dt = \partial/\partial t + \mathbf{u} \cdot \nabla$ is
158 the convective derivative. The momentum equation is written in the form

$$159 \quad \frac{D\mathbf{u}}{Dt} = \frac{1}{\rho} (-\nabla p + F_{vs}), \quad (2)$$

160 where p is the pressure,

$$161 \quad F_{vs} = \nabla \cdot (2\rho\nu\mathbf{S}) \quad (3)$$

162 is the viscous force, ν is the kinematic viscosity and the trace-less rate of strain tensor
163 is

164
$$S_{ij} = \frac{1}{2}(\partial u_i / \partial x_j + \partial u_j / \partial x_i) - \frac{1}{3} \delta_{ij} \nabla \cdot \mathbf{u}. \quad (4)$$

165 The equation for the mass fractions of each species is

166
$$\rho \frac{DY_k}{Dt} = -\nabla \cdot \mathbf{J}_k + \dot{\omega}_k, \quad (5)$$

167 where Y is the mass fraction. \mathbf{J} is the diffusive flux, $\dot{\omega}$ is the reaction rate and
 168 subscript k refers to species number. The calculation of the reaction rate $\dot{\omega}$ and
 169 diffusive flux \mathbf{J} is based on the work of Babkovskaia et al ²⁵.

170 Finally, the energy equation is

171
$$(c_p - \frac{R}{m}) \frac{D \ln T}{Dt} = \sum_k \frac{DY_k}{Dt} \left(\frac{R}{W_k} - \frac{h_k}{T} \right) - \frac{R}{W_{mix}} \nabla \cdot \mathbf{u} + \frac{2\nu S^2}{T} - \frac{\nabla \cdot \mathbf{q}}{\rho T}, \quad (6)$$

172 where T is the temperature, c_p is the specific heat at constant pressure, R is the
 173 universal gas constant, h is the enthalpy, m is the molar mass, and \mathbf{q} is the heat flux.
 174 In this work, we use the ideal gas equation of state given by

175
$$p = \frac{\rho RT}{m} \quad (7)$$

176 to enclose above equations.

177 Besides, the kinematic viscosity ν in Eq. (2) is calculated as²⁶,

178
$$\nu = \frac{1}{\rho} \sum_{k=1}^{nspec} \left[x_k \mu_k / \sum_j \left(x_j \left(\frac{1}{2\sqrt{2}} \frac{1}{\sqrt{1+m_k/m_j}} \left(1 + \sqrt{\frac{\mu_k}{\mu_j}} * \left(\frac{m_k}{m_j} \right)^{-0.25} \right)^2 \right) \right) \right] \quad (8)$$

179 **where** x_k is the species' mole fraction in the gas mixture and the dynamic viscosity
 180 of a given species μ_k is a function of local temperature as²⁷,

181
$$\mu_k = \frac{5}{16} \frac{\sqrt{\pi k_B T m_k}}{\pi \sigma_k^2 \Omega_k^{(2,2)*}} \quad (9)$$

182 **where** σ_k is the Lennard-Jones collision diameter, k_B is the Boltzmann constant.

183
$$\Omega_k^{(2,2)*} = \Omega_{L-J}^{(2,2)*} + 0.2 \delta_k^* / T_k^* \quad (10)$$

184 is the collision integral²⁸, in which,

185
$$\Omega_{L-J}^{(2,2)*} = \left[\sum_{i=0}^7 a_i (\ln T_k^*)^i \right]^{-1} \quad (11)$$

186 is the Lennard-Jones collision integral and

187
$$\delta_k^* = \frac{\nu_k^2}{2\varepsilon_k \sigma_k^3}, T_k^* = \frac{k_B T}{\varepsilon_k} \quad (12)$$

188 are the reduced dipole moment and temperature, respectively. And ε_k is the
 189 Lennard-Jones potential well depth and ν_k is the dipole moment. Both of them
 190 should be given as input together with σ_k . **The coefficients a_i can be found in the**
 191 **paper²⁵.**

192 In Eq. (4), the heat flux \mathbf{q} is given by

193
$$\mathbf{q} = \sum_k h_k \mathbf{J}_k - \lambda \nabla T, \quad (13)$$

194 where the thermal conductivity λ is found from the thermal conductivities of the
 195 individual species as

196
$$\lambda = \frac{1}{2} \left(\sum_k^{nspec} x_k \lambda_k + 1 / \sum_k^{nspec} x_k / \lambda_k \right), \quad (14)$$

197 in which the individual species conductivities

198
$$\lambda_k = \frac{\nu_k}{m_k} (f_{trans} C_{v,trans} + f_{rot} C_{v,rot} + f_{vib} C_{v,vib}) \quad (15)$$

199 are composed of transitional, rotational²⁵ and vibrational contributions²⁹.

200 The enthalpy of the ideal gas mixture, as used in Eq. (4), can be expressed in
 201 terms of isobaric specific heat and temperature as

202
$$h_k = h_k^0 + \int_{T_0}^T c_{p,k} dT, \quad h = \sum_k^{nspec} Y_k h_k \quad (16)$$

203 The heat capacity is calculated by using a Taylor expansion,

204
$$c_p = \frac{R}{m} \sum_{i=1}^5 \alpha_i T^{i-1} \quad (17)$$

205 **where α_i can be found in the CHEMKIN manual³⁰.**

206 **Ghost-cell immersed boundary method for char combustion**

207 In the previous work¹⁸, we have proposed a ghost-cell compressible immersed
 208 boundary method (GCCIB) which is capable of handling Dirichlet, Neumann and
 209 Robin boundary conditions. **In the present work, this method is further developed to**

210 involve chemical reaction inducing mass transfer processes. Its easy implementation
211 enables us to use the existing solver of the PENCIL CODE²⁴ without modifying the
212 governing equations.

213 In heterogeneous combustion context, the coupling among the boundary velocity,
214 temperature and the species mass fraction is complicated. Especially, surface reactions
215 affect mass and energy balance at the gas-solid interface, and thus have an important
216 influence on the boundary conditions. Therefore, the most difficult thing is to determine
217 the proper IB boundary conditions and then enforce them to the flow field in the present
218 method. A detailed description of the corresponding strategy can be found in the
219 following introductions.

220 A brief schematic of the reconstruction scheme in the GCCIB method¹⁸ is shown
221 in Figure 1. Three layer of ghost points is chosen to construct a six-order central finite
222 difference. Under Dirichlet boundary condition, e.g., velocity and given temperature
223 boundary conditions, a local second-order accurate extrapolation for the ghost point
224 can be obtained by using only the mirror point together with the BI point. While for
225 Neumann and Robin boundary condition, e.g., non-penetration, given heat flux and
226 chemical species boundary conditions, instead of the mirror point, two probe points
227 are needed to maintain the second-order accuracy. More details can be found in our
228 previous work¹⁸.

229 **The velocity at the immersed boundary**

230 The convective and diffusive mass flux of gas-surface species at the surface are
231 balanced by the production (or depletion) rate of gas phase species by surface reactions.
232 This relationship is

$$233 \quad \bar{n} \cdot \left[\rho Y_k (\bar{V}_k + \bar{u}) \right] = \dot{S}_k W_k, \quad (18)$$

234 where \bar{n} is the outward-pointing unit vector that is normal to the surface and \dot{S}_k is

235 the molar production rate of the k th species. Here, the gas-phase diffusion velocities are
 236 related to the gradients of species mass fraction by

$$237 \quad \bar{V}_k = \frac{1}{X_k \bar{W}} \sum_{j \neq k}^{K_g} W_j D_{k,j} \nabla X_j \quad (19)$$

238 and can be calculated from the species transport equation with

$$239 \quad \sum_k V_k Y_k = 0, \quad (20)$$

240 being a constraint for diffusion velocities of different species. The induced Stefan flow
 241 velocity is given by

$$242 \quad \bar{n} \cdot \bar{u} = \frac{1}{\rho} \sum_{k=1}^{K_g} \dot{m}_k. \quad (21)$$

243 During char combustion process, the char particle keeps shrinking and its boundary
 244 moving velocity, which is in the normal direction to the boundary, can be calculated
 245 as

$$246 \quad v_n = \frac{dr_s}{d\tau} = \frac{\int_{surf} \dot{m}_c ds}{\pi r_s \rho_c}. \quad (22)$$

247 The velocity at the interface is a combined effect of Stefan flow velocity and the particle
 248 shrinking velocity

$$249 \quad u_{IB} = \bar{u} + v_n. \quad (23)$$

250 Since the velocity at the immersed interface is now a known variable, the ghost point
 251 velocities can then be calculated using a linear interpolation as,

$$252 \quad u_G = \frac{(d_0 + d_1)u_{IB} - d_0 u_M}{d_1}, \quad (24)$$

253 where u_M is the velocity value on mirror point. The definition of d_0 and d_1 can be
 254 found in Figure 1.

255 **The temperature of the immersed boundary**

256 By neglecting the temperature gradient within the particle, the diffusive heat flux in

257 the gas phase is balanced by thermal radiation, chemical heat release and heat
 258 conduction from the gas phase to the solid surface, such that

$$259 \quad Vc_{p,c} \frac{dT_p}{d\tau} = \int_{Surf} \left(-\sigma\varepsilon(T_p^4 - T_0^4) + \sum_{k=1}^K \dot{m}_k h_k + \bar{n} \cdot \lambda \nabla T_{gas} \right) ds, \quad (25)$$

260 where V is the volume of the object and the integral on the right hand side is over the
 261 external surface of the object while ds is a surface element. T_0 is the temperature of
 262 surrounding gas. The calculation of the enthalpy is based on the form used in
 263 CHEMKIN³⁰. In this work, Equation (18) is solved explicitly to only obtain the time
 264 history of particle temperature and not to implement the thermal boundary conditions.
 265 On the chemically reacting surface, the temperature gradient should be prescribed³¹,
 266 i.e., a Neumann type temperature boundary condition is necessary.

267 **The enforcement of species boundary condition**

268 Species concentrations are unknown variables at the immersed interface. Due to
 269 the fact that heterogeneous reactions affect the mass and energy balance at the
 270 interface, they have a significant influence on the boundary conditions both for the
 271 gas species and for the temperature.

272 The convective and diffusive mass fluxes of the gas phase species at the particle
 273 surface are balanced by the production/destruction rates of gas phase species by
 274 surface reactions,

$$275 \quad \rho D_k \bar{n} \cdot \nabla Y + \dot{m}_c Y_k + \dot{m}_k = 0 \quad (26)$$

276 where the first term represents the diffusive mass flux while the second term is the
 277 convective mass flux and \dot{m}_k is the mass production rate of the k th species. A
 278 detailed deduction of Eq. (26) can be found in Appendix B. The diffusion coefficient
 279 D_k is calculated in a simple way as CHEMKIN³⁰,

$$280 \quad D_k = \frac{D_{const}}{\rho} \cdot \left(\frac{T_{IB}}{T_{ref}} \right)^{0.7} \cdot \frac{1}{Le_k} \quad (27)$$

281 where $D_{const} = 2.58 \times 10^{-4} \text{ kg / (m} \cdot \text{s)}$ and $T_{ref} = 298 \text{ K}$.

282 According to Eq.(26), the species at the burning boundary follows the
283 representation of Robin type boundary condition. The only unknown parameters are
284 the mass production rates \dot{m}_C and \dot{m}_k . Since \dot{m}_C and \dot{m}_k are coupled with the
285 species mass fraction Y_k , Eq.(26) is supposed to be solved implicitly. While in the
286 present work, the mass fraction Y_k at the immersed boundary is calculated by
287 bilinear-interpolate the mass fraction of current time-step on surrounding fluid points,
288 which means that Eq.(26) is solved explicitly here. Details about the calculation of
289 mass fractions at the ghost point can be found in Appendix B.

290 **The enforcement of pressure boundary condition**

291 The pressure gradient in the vicinity of the immersed boundary needs to be zero
292 to fulfill the non-penetration condition and this is implemented through the
293 reconstruction of the density by applying the equation of state. A second-order
294 expression can be written as

$$295 \quad \rho_G = \frac{m_G}{T_G} \left[\frac{\rho_1 T_1}{m_1} + \frac{d_0^2 - d_1^2}{d_2^2 - d_1^2} \cdot \left(\frac{\rho_2 T_2}{m_2} - \frac{\rho_1 T_1}{m_1} \right) \right], \quad (28)$$

296 where the subscript G denotes ghost point and 1(or 2) indicates the information on the
297 first (or the second) probe point. d_0 , d_1 and d_2 are defined in Figure1. The
298 calculation of the ghost point density can be found in Appendix B.

299 **A summary of the present method**

300 In every time step, the novel ghost cell immersed boundary method for gas-solid
301 multiphase combustion can be summarized as follows:

- 302 (1) Detect the position of the immersed interface and identify the ghost points,
303 boundary intersection points, mirror points and probe points;
- 304 (2) Calculate the production rate \dot{m}_C and \dot{m}_k at the immersed boundary using the

305 Arrhenius equation and get the mass fractions at the ghost points with the Robin
306 type reconstruction scheme;

307 (3) Calculate the Stefan flow velocity and particle shrinking velocity with the
308 production rate \dot{m}_C and \dot{m}_k ;

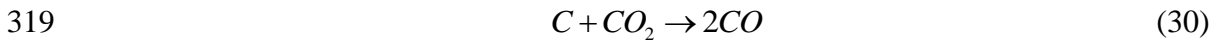
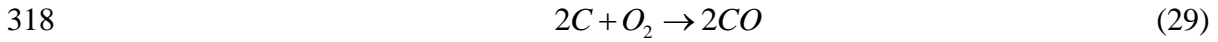
309 (4) The particle temperature at the next time step can be found explicitly through Eq.
310 (25), using the temperature of the present time step in the RHS of the equation;

311 (5) Compute the ghost cell values for all variables and update the particle radius
312 according to the particle shrinking velocity.

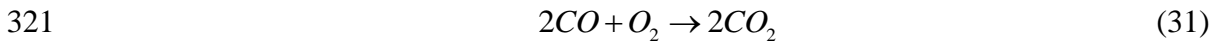
313 **Problem and assumptions**

314 In the present work, a single cylindrical char particle, placed in a free gaseous
315 flow, was considered. The chemistry was modelled using semi-global homogeneous
316 and heterogeneous reactions written as follows.

317 *Heterogeneous reactions:*



320 *Homogeneous reaction:*



322 The reaction kinetics parameters are listed in Table 1.

323 The heterogeneous char reaction rates are assumed to be of first order both in
324 oxygen and carbon dioxide concentration. Hence, the reaction rates of O_2 , CO_2 and CO
325 due to the heterogeneous reactions can be written as

$$326 \quad \dot{m}_{O_2} = -\rho Y_{O_2} B_1 \exp\left(-\frac{E_1}{RT_p}\right), \quad (32)$$

$$327 \quad \dot{m}_{CO_2} = -\rho Y_{CO_2} B_2 \exp\left(-\frac{E_2}{RT_p}\right), \quad (33)$$

$$328 \quad \dot{m}_{CO} = -2\left(\frac{M_{CO}}{M_{O_2}} \dot{m}_{O_2} + \frac{M_{CO}}{M_{CO_2}} \dot{m}_{CO_2}\right). \quad (34)$$

329 Then, the char conversion rate can be calculated as

$$330 \quad \dot{m}_c = 2 \frac{M_c}{M_{O_2}} \dot{m}_{O_2} + \frac{M_c}{M_{CO_2}} \dot{m}_{CO_2}. \quad (35)$$

331 To simulate the char conversion process with the present ghost-cell immersed
332 boundary method, several assumptions and simplifications are needed, which are listed
333 below.

- 334 1) The porosity of the particle is incorporated into the pre-exponential factors of the
335 heterogeneous reactions;³²
- 336 2) The cross section of particle is circular during the shrinking process;
- 337 3) The particle consists of carbon only;
- 338 4) The temperature gradient within the particle is neglected;
- 339 5) The gaseous environment only consists of N₂, O₂, CO and CO₂. Water vapor is
340 taken into account by having an effect on the CO oxidation reaction;³²
- 341 6) The gas radiation is not taken into account.

342 In the present simulation, the particle oxidation only happens at the particle
343 surface. The shape of the particle remains circular during the shrinking process for
344 easy interface tracking. According to these assumptions, the chemical reactions only
345 happen at or outside the solid-fluid interface.

346 Numerical results

347 Convergence test

348 Since the spatial accuracy for no-slip velocity, non-impermeable pressure and
349 Dirichlet, Neumann and Robin thermal boundary conditions has been presented in our
350 previous work¹⁸, we focus on the Robin type reactive boundary condition in this
351 paper.

352 The case of a 2D char particle burning in a quiescent atmosphere is conducted to

353 verify that the present scheme is of second order spatial accuracy. The solid particle is
354 located at the center of a square computational domain with the size of $10d \times 10d$ (d
355 is the diameter of the cylinder). A series of grid resolutions
356 (400×400 , 600×600 , 800×800 and 1600×1600) are used to calculate the same
357 problem. Periodic boundary conditions are enforced on both the streamwise and
358 spanwise directions. We choose a relatively small time step of 2×10^{-8} s and integrate
359 the solution to the same instant (0.01s) for all resolutions. The results with the highest
360 resolved grid of 1600×1600 is used as a baseline.

361 Figure 2 shows the variation of the norms of relative errors and indicates the
362 accuracy of the scheme. The mass fractions of species N_2 , CO and CO_2 (not
363 considering O_2 is due to the almost zero value because O_2 is consumed completely in
364 the CO flame sheet) in the vicinity of the solid surface are used to calculate the
365 L_2 -norm errors, because we mainly care about the accuracy near the IB. As we can
366 see from Figure 2, the second order convergence accuracy is achieved for all species.

367 **Validation**

368 In the previous work¹⁸, the ability of the present method to handle Dirichlet,
369 Neumann and Robin type thermal boundary condition has been validated. In this
370 section, the GCCIB method is first used to simulate the experiment conducted by
371 Makino et al³² for validation of its capability to deal with a reacting surface. Figure 3
372 describes the experimental setup, where a graphite rod with the diameter $d = 5$ mm and
373 density $\rho = 1.25 \times 10^3$ kg/m³ is placed in air atmosphere. The hot oxidizing gas flows
374 toward the cylinder at different speeds and the average consumption rate of the
375 specimen is measured.

376 In the simulation, a large $20d \times 16d$ computational domain (see Figure 4) is
377 adopted to minimize domain confinement effects and the grid resolution is chosen to

378 be $\Delta x = 1/50d$. The inlet temperature of the oxidizing gas is set to be 1280K and the
379 incoming velocity is defined by the velocity gradient $a = 4V_\infty / d$, which is $820s^{-1}$
380 in the current paper. The pressure at the inlet is $p_0 = 1.01 \times 10^5 Pa$. As shown in Figure
381 4, NSCBC³³ boundary conditions are applied at both the inlet and outlet boundary
382 while periodic boundary conditions are used for the span wise direction. Every
383 simulation runs for 0.1s so that a quasi-steady state can be obtained.

384 First, the evolution history of the temperature of the graphite rod is investigated in
385 Figure 5. As can be seen, the temperature keeps decreasing during the simulation and
386 the amplitude is within 30K, as a result of the energy balance of reactive heat release,
387 conduction, convection and radiation heat transfer. This was confirmed by the
388 experimental observation of Makino et al³² that the rod needed to be heated by a
389 resistive heater to remain at a constant temperature. Therefore, in the following
390 simulations, the solid surface temperature is fixed.

391 In Figure 6, the conversion rate of the carbon cylinder, calculated by the current
392 method, is compared with the experimental measurement and analytical results³². In
393 view of all the assumptions and uncertainties, the error is acceptable. Moreover, one
394 can see that with the increase of surface temperature, the combustion rate first increases,
395 then decreases, and then increases again. This transition phenomenon in the variation of
396 carbon burning rate with the increase of surface temperature is accurately captured and
397 the critical temperature is about 1700K, which is agreeing well with the experimental
398 result.

399 There are various explanations for this transition phenomenon, such as the “site”
400 theory³⁴ and the change of reaction depth at constant activation energy³⁵. Makino et al³⁶,
401 however, attributed it to a change of the dominant surface reaction from R1
402 ($2C-O_2 \rightarrow 2CO$) to R2 ($C-CO_2 \rightarrow 2CO$), which is caused by the appearance of a CO flame

403 over the burning carbon. With the current access to fully-resolved simulations of the
404 relevant cases, the underlying physical reason for the transition phenomena is explored.

405 Figure 7 shows the CO flame in terms of the consumption rate of carbon monoxide
406 by the homogenous reaction. With the increase of surface temperature, a CO flame
407 starts to form in front of the cylinder and then wraps the rod while staying attached to
408 the solid surface. When the surface temperature exceeds 1700K, the flame first
409 detaches from the rear of the rod and then from the front. Finally, a CO flame sheet is
410 formed around the solid surface at a given distance. It prevents the oxygen from
411 diffusing to the carbon surface, and hence, causes an increase in the relevance of R2 at
412 the expense of R1. The change of the flame structure is a result of the competition
413 between the incoming flow and the Stefan flow. Figure8 shows the respective
414 contribution of O₂ and CO₂ to the production of CO in heterogeneous reactions. The
415 transition from solid carbon oxidation to gasification is evident. Present results agree
416 well with Makino's conclusions³⁶. This provides a validation of the applicability of
417 the present surface resolved IB method for detailed descriptions of char particle
418 conversion.

419 **Study of transport and chemistry interactions**

420 In this section, the influence of the flow field on properties of single char particle
421 conversion will be investigated by analyzing results from cases with different particle
422 Reynolds numbers. Then, the effect of the char conversion on particle drag force and
423 heat transfer with surrounding fluid will be studied. Both of the above points are of
424 vital importance in modeling reactive particulate flows.

425 The particle Reynolds number is varied from 2.5 to 30.0 (Re=2.5, 5, 7.5, 8, 15,
426 20, 25, 30.0.), by changing the velocity of the incoming flow. The lower range (2.5 to
427 8.0) of the Reynolds number is chosen based on the conditions in Aachen's 100 kW

428 swirl burner³⁷. What demand add is that, the diameter is set to be 5mm in the present
429 simulation. Although this doesn't match the condition in Aachen swirl burner where
430 the particle size ranges from 4.5um to 435um, we keep the dimensionless Reynolds
431 number the same by using the non-dimensionalization. For investigation of the drag
432 force and heat transfer, this is meaningful. The upper range (8.0 to 30.0) is to make a
433 full use of current simulation data. The solid surface temperature is fixed at 1500K to
434 keep the gas reaction zone constrained near the solid surface. Otherwise, the
435 simulation setup is the same as that described in the validation section. Each
436 simulation runs for 0.1s to ensure that a quasi-steady state has been obtained. Density,
437 porosity and diameter variations can be neglected for this small time period compared
438 with the whole burnout time.

439 **Conversion properties under different Reynolds numbers**

440 In this section, both char conversion and the gas phase reactions are analyzed.
441 The influence of particle Reynolds number on the averaged consumption rate over the
442 surface of the char particle is plotted in Figure 9. An increase of the char conversion
443 rate with increasing Reynolds number can be observed, as is also found by Richter
444 et.al³⁸. Because the temperature of the solid surface is fixed, we explore the behind
445 reasons by quantifying the mass fraction of different species at the solid surface in
446 Figure 10. As can be seen, with the increase of Reynolds number, the averaged
447 concentration of oxygen over the solid surface increases while the concentration of
448 carbon dioxide decreases. Since char conversion due to oxidation dominates within
449 the current range of Reynolds number, an increase of the conversion rate is reasonable.
450 Due to the relatively high activation energy of the gasification reaction, it could be
451 expected that at higher surface temperature, when the relative importance of
452 gasification increases (see Figure 8), the Reynolds number trend shown in Figure 7

453 will be weakened. To understand the underlying reasons that result in such a
454 distribution of oxygen and carbon dioxide, the respective diffusive and convective
455 fluxes of O₂ and CO₂ are investigated. Both of the two quantities are averaged over
456 the particle surface and defined as positive away from the interface. Figure 11 shows
457 the variation of these quantities with increasing Reynolds numbers. It can be observed
458 that diffusion dominates for the transportation of oxygen towards the surface while
459 convection takes advantage over diffusion to transport carbon dioxide away from the
460 fluid-solid interface. Since a higher Reynolds number means faster transportation of
461 oxygen from the incoming flow to the border of the burning boundary layer and also
462 thinner boundary layer, which leads to sharper gradient of the concentration of O₂, a
463 rapid diffusion of O₂ through the layer can be expected. As a result, the carbon is
464 consumed more rapidly, resulting in a faster Stefan flow (see Eq (21)). This
465 contributes significantly to the convection of CO₂ away from the solid surface.
466 Moreover, one can see that carbon monoxide is transported away from the solid
467 surface by both convection and diffusion, indicating that the heterogeneous reactions
468 are providing reactants to the gas-phase reaction.

469 Similar to the effect of an increasing surface temperature, the increasing particle
470 Reynolds number also contributes to a change in the relative importance of the
471 oxidation and gasification reactions, which can be seen in Figure 12. This is a result of
472 a different dominant factor (for the respective transportation of O₂ and CO₂). High
473 Reynolds number increases the diffusion of oxygen to the solid surface while the
474 resulting faster Stefan flow transports more carbon dioxide away from the surface.
475 Figure 12 also implies that the single-film model is appropriate for char particle
476 combustion when the Reynolds number is high.

477 The reaction zones of the gas phase for different Reynolds numbers are shown in

478 Figure 13 in terms of the consumption rate of carbon monoxide by the homogenous
 479 reaction. A difference from the varying surface temperature situation, is that the
 480 structure of the reactive zone does not change much with increasing Reynolds number,
 481 while the maximum reaction rate goes up, especially at the front stagnation point
 482 where the most violent reaction of gas phase occurs. Except for the contribution from
 483 an increase of the CO production from the surface reactions, the distribution of the
 484 Damköhler number (Da) in Figure 14 shows that both the convective and diffusive
 485 Damköhler number is always above one, meaning that the gas phase reaction is
 486 always transport-limited, and thus an increase of the velocity of incoming flow will
 487 provides much more oxygen to this reaction, leading to a faster gas phase reaction.
 488 Here, the convective Da is defined as

$$489 \quad Da_{conv} = \frac{\tau_{conv}}{\tau_{chem}}, \quad (36)$$

490 where τ_{conv} is the convective time scale, defined as

$$491 \quad \tau_{conv} = \frac{d_p}{U_\infty}. \quad (37)$$

492 The diffusion Da is

$$493 \quad Da_{diff} = \frac{\tau_{diff}}{\tau_{chem}}. \quad (38)$$

494 And

$$495 \quad \tau_{diff} = \frac{d_p^2}{D_{CO}} \quad (39)$$

496 is diffusion time scale with D_{CO} being the CO diffusion coefficient in gas mixture.

$$497 \quad \tau_{chem} = \frac{Y_{CO}}{R_{(3)}} \quad (40)$$

498 is the characteristic time for chemistry. Another point worth of noting is that when the
 499 Reynolds number is above 5, the transport is controlled by diffusion instead of

500 convection.

501 To investigate the local char conversions, three different angular positions at the
502 surface are chosen for closer inspection. In Figure 15, the conversion rates of different
503 species at the three angular positions are shown. Consistent with CO gas-phase
504 conversion in the boundary layer, the stagnation point is still the most reactive zone for
505 heterogeneous reactions. It is also seen that the reaction at the rear stagnation point is
506 not sensitive to the Reynolds number.

507 **Effect of combustion on mass, momentum and energy exchange**

508 With heterogeneous and homogeneous reactions occurring on the solid surface
509 and in the bulk gas, the temperature and species concentration in the gas mixture near
510 the particle surface show a behavior that is different from a non-reactive situation.
511 Hence, the fluid properties, such as dynamic viscosity and thermal conductivity, vary
512 accordingly. In addition, the Stefan flow also changes the flow structure, leading to
513 quite different velocity and temperature gradient distributions over the particle.
514 Therefore, char conversion rates are expected to have a significant influence on both
515 the drag force and the Nusselt number, which are the two main parameters used to
516 calculate the exchange of momentum and energy between gas and solid phase. This
517 effect is investigated in the following.

518 The drag force coefficient

$$519 \quad c_d = \frac{F_{drag}}{\frac{1}{2} \rho U_\infty^2} \quad (41)$$

520 and the Nusselt number

$$521 \quad Nu = \frac{\int_{surf} \nabla T \cdot \vec{n} ds}{T_s - T_\infty} \quad (42)$$

522 for situations with and without heterogeneous reactions are shown in Figure 16. The
523 corresponding c_d and Nu from Triton's experimental results³⁹ and Churchill and

524 Bernstein's correlation function ⁴⁰

$$525 \quad Nu = 0.3 + \frac{0.62 Re^{1/2}}{\left[1 + (0.4 / Pr)^{2/3}\right]^{1/4}} \left[1 + \left(\frac{Re}{282000}\right)^{5/8}\right]^{4/5} \quad (43)$$

526 are also shown, respectively. It can be observed that the present non-reactive results
527 (obtained by turning off the heterogeneous reactions) agree well with that in
528 literatures. With a reactive solid surface, the drag force coefficient follows the same
529 trend with increasing Reynolds number compared to that in the non-reactive situation.
530 However, the magnitude is much higher. The underlying physical reasons are first
531 investigated by comparing the averaged gas-phase viscosity (averaged over a
532 $4d \times 4d$ square domain with the cylinder occupation excluded) and comparing them
533 with the that for air at 1280K and under 1 bar atmosphere. As is shown in Table. 2, the
534 gas mixture becomes more viscous in the reactive situation due to the change of the
535 mixture components and also the higher temperature. Other contributions to the
536 increase of the drag force may include the change of the hydrodynamic boundary
537 layer around the particle caused by the Stefan flow, as is shown by Dierich et al²³. As
538 a result of the heat release by gas-phase combustion in the boundary layer, a high
539 temperature zone (shown in Figure 17) forms around the particle, resulting in a strong
540 heat flux towards the solid surface, as is described by Figure 16. Moreover, a faster
541 gas-phase reaction with a higher Reynolds number releases more heat, leading to a
542 larger value of the Nusselt number. Finally, the evolution of the Sherwood number
543 which is defined as

$$544 \quad Sh = \frac{\int_{Surf} \left(\sum_i^k \rho D_i \nabla Y_i \right) ds}{\rho \pi d \sum_i^k D_i (Y_{inlet,i} - Y_{surf,i})} \quad (44)$$

545 is investigated in Figure 16. With increasing Reynolds number, the Sherwood number
546 decreases, implying that to eject the same amount of mass into the gas flow more gas

547 is transported to the solid surface and thus a low mass conversion efficiency.

548 **Discussions and conclusions**

549 In this work, a novel ghost-cell immersed boundary method is proposed to
550 describe the process of carbon burning. A convergence test shows that the current
551 method can obtain a local second-order spatial accuracy. By comparing results from
552 the present simulations with corresponding experimental results, the capability and
553 accuracy of the present method is validated. The jump of the combustion rate of the
554 graphite rod at about 1700K is successfully captured. The physical reasons behind this
555 phenomenon are explored. The change of the CO flame structure can be clearly
556 observed, and consequently, the dominant surface reaction changes gradually from
557 oxidation to gasification with increasing surface temperature. These findings agree
558 well with conclusions by Makino et al³², providing some validation that the present
559 particle resolved IB method is suitable for a further investigation of char combustion.
560 The results also imply that the double-film model may be more suitable than the
561 single-film model when the surface temperature is high. Notably, Hecht et al⁴¹,
562 Gonzalo-Tirado et al^{42, 43} and Farazi et al⁴⁴ also pointed out that the single-film
563 assumption fails for large particles like that in the present simulation.

564 Based on the validations mentioned previously, the interaction between CO₂
565 gasification and O₂ oxidation introduced by varying Reynolds number are
566 investigated as well as other char conversion properties. Results show that with
567 increasing Reynolds number the contribution of O₂ oxidation to char consumption
568 becomes more significant and the conversion rate of the char particle rises. By
569 comparing this trend with the effect of surface temperature, it can be concluded that
570 the solid surface temperature dominates over the Reynolds number when it comes to
571 how to choose between single-film and double-film models for char conversion.

572 Specifically speaking, the leading edge of the cylinder is the most reactive position for
573 both surface and gas-phase chemistry. In the range of Reynolds numbers studied here,
574 the gas phase reaction in the boundary layer is always transport-limited such that
575 higher Reynolds numbers results in faster combustion.

576 Moreover, the effect of combustion on the exchange of mass, momentum and
577 energy between gas- and solid-phase is explored. Computational data indicates that a
578 larger drag force is exerted on a solid particle that is embedded in a reactive
579 environment. Heat release from the combustion in the boundary layer generates a high
580 temperature sheet around the solid surface, causing a strong heat flux toward the
581 burning surface. Even though, in the validation part, one can see that the solid surface
582 temperature keeps decreasing, which means that radiation cannot be ignored in the
583 energy conservation equation for the solid particle. By analyzing the Reynolds
584 number dependence on the Sherwood number, one can find that higher Reynolds
585 numbers lead to lower mass transfer efficiency, even with a fast char conversion rate.

586 It is concluded that the present GCCIB method is a powerful tool for fully
587 resolved simulations of gas-solid flows with heterogeneous reactions. With the
588 detailed information provided by such a simulation, one can improve the existing char
589 conversion model and even develop new models. In the future, an extension of the
590 present method to 3D particles under various conditions, such as oxy-fuel combustion
591 and more detailed chemical mechanisms, will be explored.

592 **Acknowledgement**

593 This work is supported by the National Natural Science Foundation of China (Nos. 51390490).

594 **Appendix A**

595 The burning solid surface is like the following Figure18, where the symbol (+) and
596 (-) indicate the direction of mass flux of a given species.

597 With Fick's law applied on the surface, one has

$$598 \quad \vec{m}_k = Y_k \vec{m}_{net} - \rho D \nabla Y_k \quad (45)$$

599 where \vec{m}_k denotes the mass flux of species k and \vec{m}_{net} is the bulk mass flux.

$$600 \quad \nabla Y_k = \frac{\partial Y_k}{\partial r} \quad (46)$$

601 is the gradient of the mass fraction of species k along the normal direction of the
602 surface.

603 In the present case, \vec{m}_{net} can be expressed as follows,

$$604 \quad \vec{m}_{net} = \vec{m}_{O_2} + \vec{m}_{CO_2} + \vec{m}_{CO}. \quad (47)$$

605 Due to the surface reaction (29), the consumption rate of carbon (kg/m²/s):

$$606 \quad R_{C,1} = 2k_{f,1} MW_C [O_2]_s. \quad (48)$$

607 The consumption rate of oxygen (kg/m²/s):

$$608 \quad R_{O_2,1} = k_{f,1} MW_{O_2} [O_2]_s = \frac{MW_{O_2}}{2MW_C} R_{C,1}. \quad (49)$$

609 The production rate of carbon monoxide (kg/m²/s):

$$610 \quad R_{CO,1} = 2k_{f,1} MW_{CO} [O_2]_s = \frac{MW_{CO}}{MW_C} R_{C,1}, \quad (50)$$

611 where,

$$612 \quad k_{f,1} = B_1 \exp\left(-\frac{E_1}{R_u T_s}\right). \quad (51)$$

613 MW_C , MW_{O_2} and MW_{CO} are molar weight of C, O₂ and CO, respectively. The

614 symbol $[O_2]_s$ indicates the molar concentration (mol/m³) of O₂ at the solid surface

615 and can be calculated from mass fraction of oxygen $Y_{O_2,s}$ as

$$616 \quad [O_2]_s = \frac{MW_{mix}}{MW_{O_2}} \frac{P}{R_u T_s} Y_{O_2,s} = \frac{\rho_{mix}}{MW_{O_2}} Y_{O_2,s}. \quad (52)$$

617 By analogy, due to the CO₂ gasification (30), the consumption rate of carbon

618 (kg/m²/s):

$$619 \quad R_{C,2} = k_{f,2} MW_C [CO_2]_s. \quad (53)$$

620 The consumption rate of CO₂ (kg/m²/s):

$$621 \quad R_{CO_2,2} = k_{f,2} MW_{CO_2} [CO_2]_s = \frac{MW_{CO_2}}{MW_C} R_{C,2} \quad (54)$$

622 The production rate of CO (kg/m²/s):

$$623 \quad R_{CO,2} = 2k_{f,2} MW_{CO} [CO_2]_s = \frac{2MW_{CO}}{MW_C} R_{C,2} \quad (55)$$

624 By adding Eq (48) and Eq (53), the total consumption rate of carbon can be
625 obtained as

$$626 \quad R_C = \frac{2MW_C}{MW_{O_2}} \rho_{mix} Y_{O_2,s} k_{f,1} + \frac{MW_{CO_2}}{MW_{O_2}} \rho_{mix} Y_{CO_2,s} k_{f,2} \cdot \quad (56)$$

627 Taking the outward direction to be positive and \vec{r} as the corresponding unit vector,
628 the consumption or production rate of a given species can be related to its mass flux as,

$$\begin{aligned} 629 \quad \vec{m}_{O_2} &= -R_{O_2,1} \vec{r} \\ \vec{m}_{CO_2} &= -R_{CO_2,2} \vec{r} \\ \vec{m}_{CO} &= (R_{CO,1} + R_{CO,2}) \vec{r} \end{aligned} \quad (57)$$

630 Substituting Eq (49-50) and Eq(54-55) into Eq (57) and Eq (57) into Eq (47), one has

$$631 \quad \vec{m}_{net} = R_C \vec{r} \cdot \quad (58)$$

632 By defining

$$633 \quad \vec{m}_C = R_C \vec{r} \cdot \quad (59)$$

634 the boundary condition for every species in the form of Eq (26) can be obtained. An
635 extension to reactions with more components is straightforward.

636 **Appendix B**

637 In order to maintain the second-order accuracy for the present immersed boundary
638 method, we proposed a second-order formula

$$639 \quad \varphi = a + bx + cx^2 \quad (60)$$

640 for the calculation of ghost point values. By using the given variables at the probe
641 points and the boundary condition, three parameters of the Equation (60) can be
642 calculated.

643 For the ghost point density calculation, the given condition can be written as

644 where $x = 0$, $\frac{\partial P}{\partial n} = 0$, (61)

645 where $x = d_1$, $P_1 = a + cd_1^2$, (62)

646 where $x = d_2$, $P_2 = a + cd_2^2$. (63)

647 Thus the parameters can be written as

648 $b = 0$, (64)

649 $c = \frac{P_2 - P_1}{d_2^2 - d_1^2}$, (65)

650 $a = P_1 - cd_1^2$. (66)

651 As for the mass fractions at the ghost points, the situation will be much more
 652 complicated. Since the mass fraction boundary condition is of Robin type, the given
 653 boundary condition can be listed as

654 where $x = 0$, $\rho Db + \dot{m}_c a = -\dot{m}_i$, (67)

655 where $x = d_1$, $Y_1 = a + bd_1 + cd_1^2$, (68)

656 where $x = d_2$, $Y_2 = a + bd_2 + cd_2^2$. (69)

657 and then the parameters can be represented as

658 $b = \left(-\frac{\dot{m}_i}{\dot{m}_c} - Y_1 + \frac{Y_2 - Y_1}{d_2^2 - d_1^2} d_1^2 \right) / \left(\frac{-d_1 d_2}{d_1 + d_2} + \frac{\rho D}{\dot{m}_c} \right)$, (70)

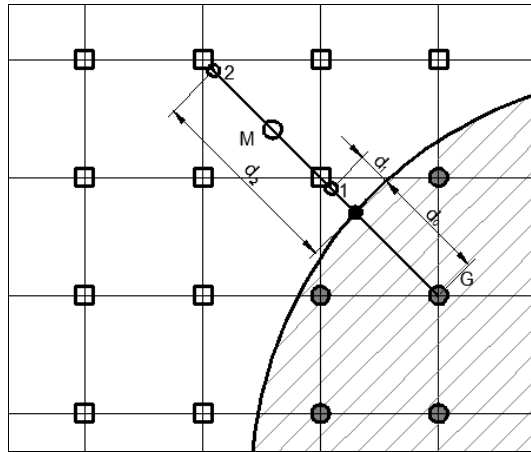
659 $a = \frac{-\dot{m}_i - \rho Db}{\dot{m}_c}$, (71)

660 $c = \frac{Y_2 - Y_1 - b(d_2 - d_1)}{d_2^2 - d_1^2}$. (72)

661 After the determination of the parameters, the ghost point variables at $x = -d_0$ can
 662 then be determined.

663

664



665

666 **Figure 1.** Extrapolation implementation for the present ghost-cell immersed boundary

667 method. (◐ : ghost points, ◐ (M): mirror points, ◐ (1, 2): probe points, ● : boundary

668 intersection (BI) points, ◐ : fluid points.)

669

670

671

672

673

674

675

676

677

678

679

680

681

682

683

684

685

686

687

688

689

690

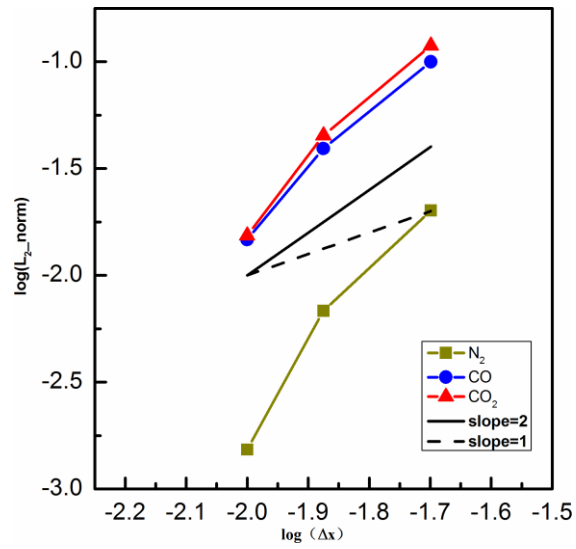


Figure 2. L_2 -norms computed at different grid levels

691
692

693

694

695

696

697

698

699

700

701

702

703

704

705

706

707

708

709

710

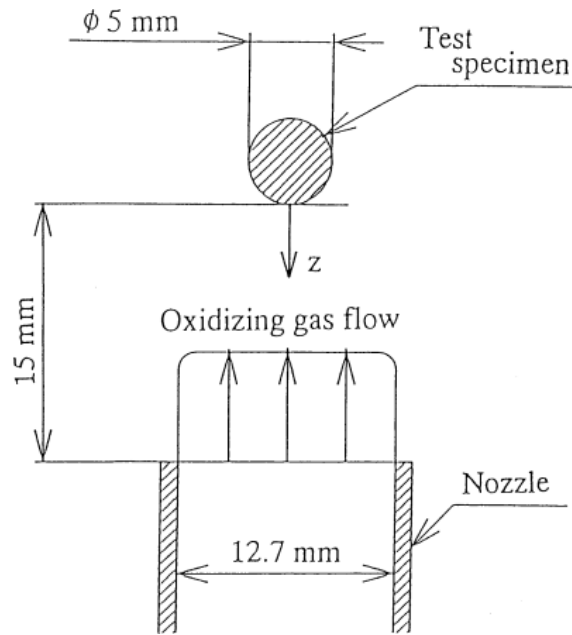
711

712

713

714

715



716

717

Figure 3. Schematic of the experiment by Makino et al ³²

718

719

720

721

722

723

724

725

726

727

728

729

730

731

732

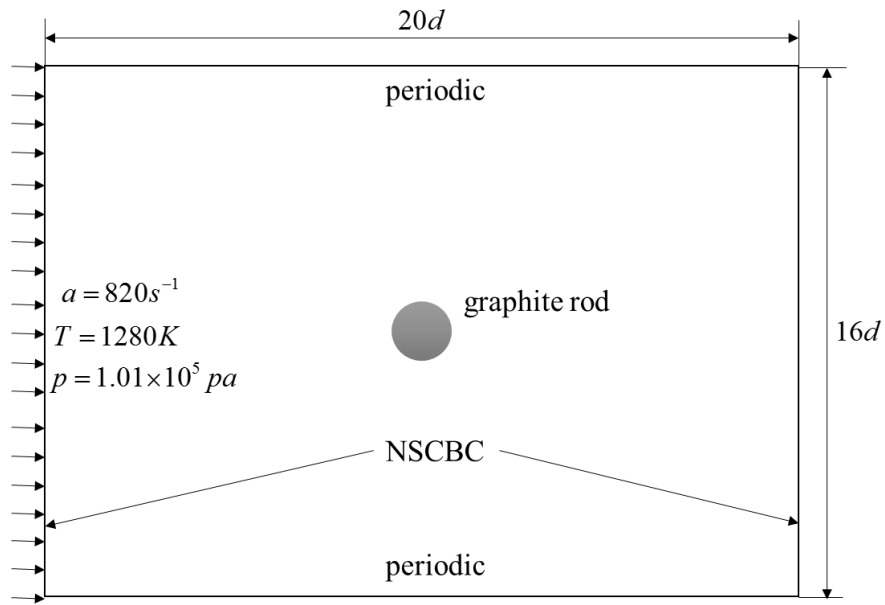
733

734

735

736

737



738

739

Figure 4. Schematic of computational domain

740

741

742

743

744

745

746

747

748

749

750

751

752

753

754

755

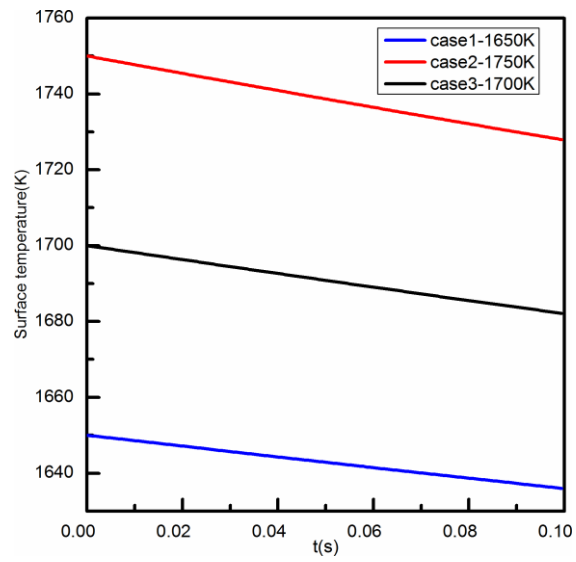
756

757

758

759

760



761

762

Figure 5. Temperature evolution of the graphite rod during combustion

763

764

765

766

767

768

769

770

771

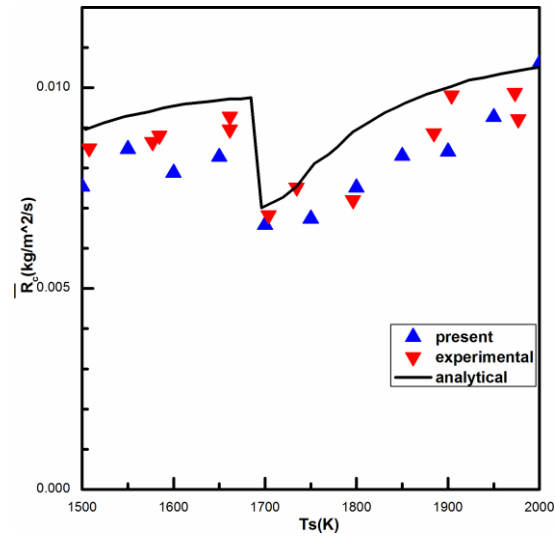
772

773

774

775

776



777

778

Figure 6. Carbon burning rate at different surface temperatures

779

780

781

782

783

784

785

786

787

788

789

790

791

792

793

794

795

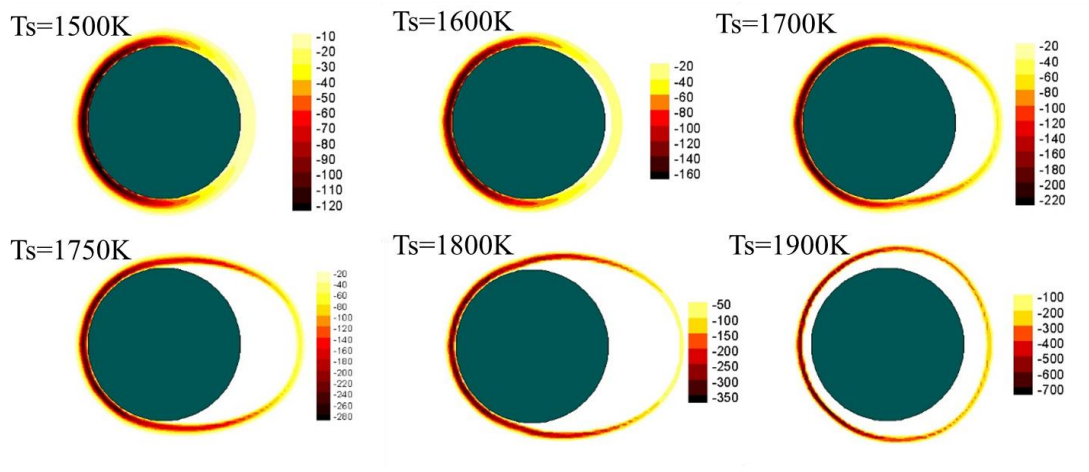
796

797

798

799

800



801

802 **Figure 7.** CO flame around the burning carbon surface at different temperatures

803

804

805

806

807

808

809

810

811

812

813

814

815

816

817

818

819

820

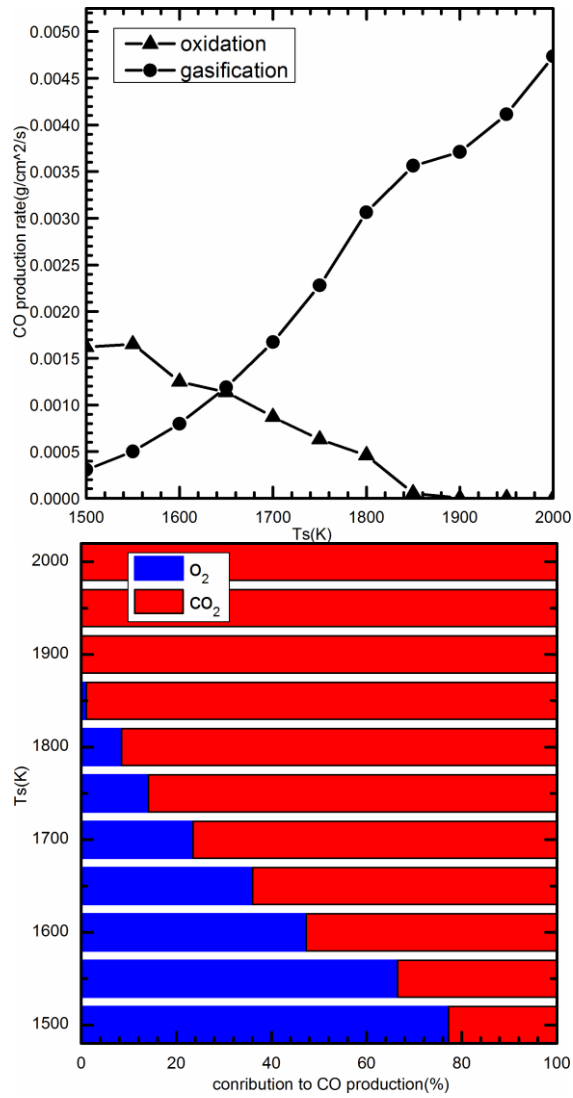
821

822

823

824

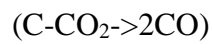
825



826

827

828 **Figure 8.** The dominant surface reaction changing from R1 ($2C-O_2 \rightarrow 2CO$) to R2



830

831

832

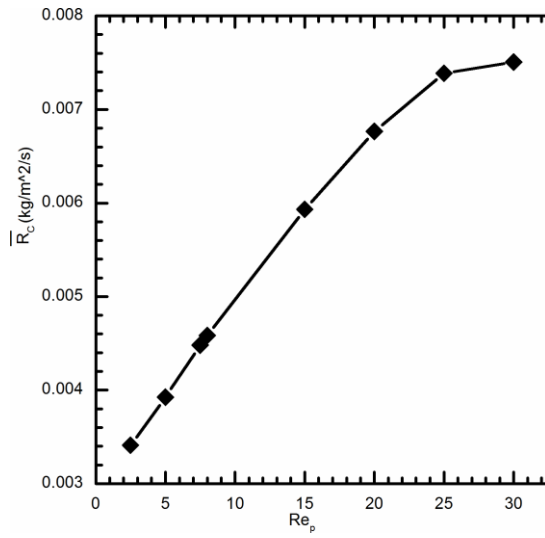
833

834

835

836

837



838

839

Figure 9. Evolution of averaged char consumption rate versus Reynolds number

840

841

842

843

844

845

846

847

848

849

850

851

852

853

854

855

856

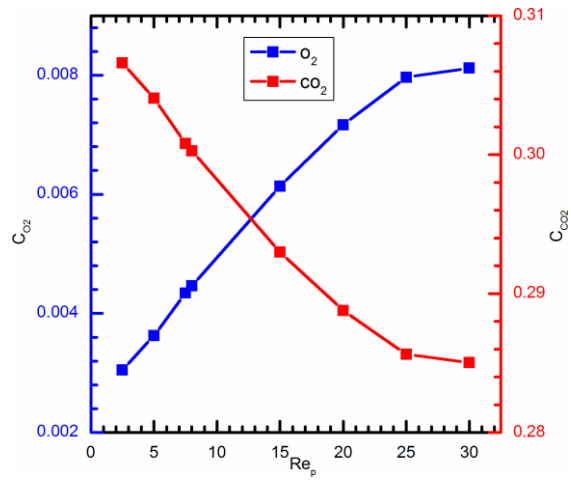
857

858

859

860

861



862

863

Figure 10. The averaged concentration of O_2 and CO_2 under different Re_p s

864

865

866

867

868

869

870

871

872

873

874

875

876

877

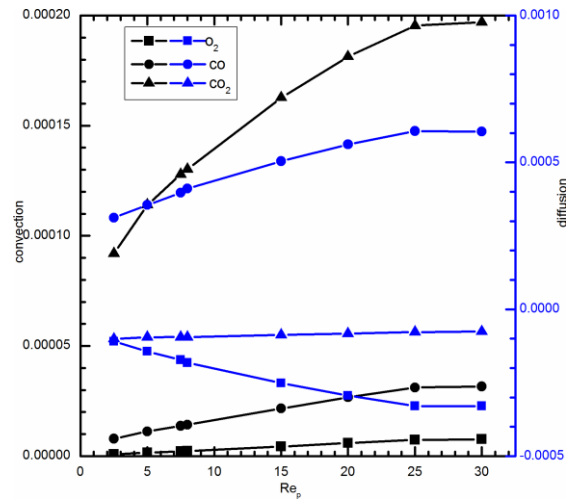
878

879

880

881

882



883

884

Figure 11. The influence of Reynolds number on averaged transportation

885

886

887

888

889

890

891

892

893

894

895

896

897

898

899

900

901

902

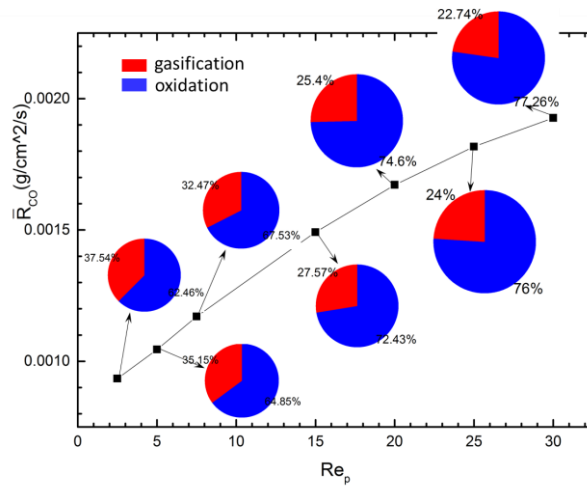
903

904

905

906

907



908

909

Figure 12. Respective contribution of O₂ and CO₂ to the production of CO on the surface

910

911

912

913

914

915

916

917

918

919

920

921

922

923

924

925

926

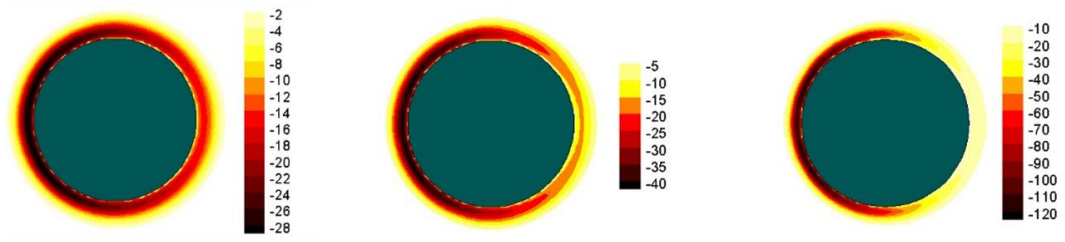
927

928

929

930

931



932

933

Figure 13. Reactive zones of gas-phase in terms of CO consumption rate

934

935

936

937

938

939

940

941

942

943

944

945

946

947

948

949

950

951

952

953

954

955

956

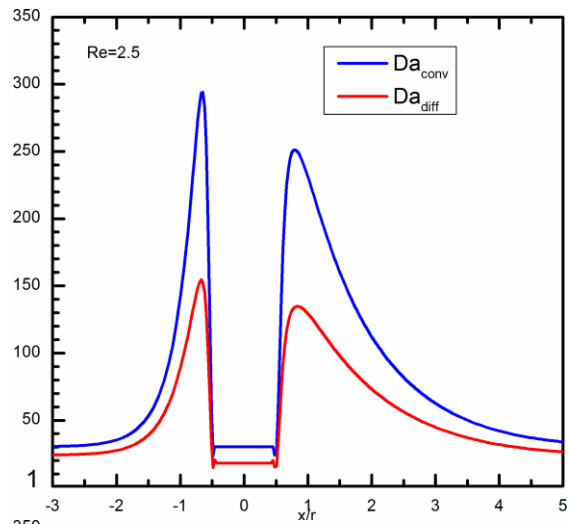
957

958

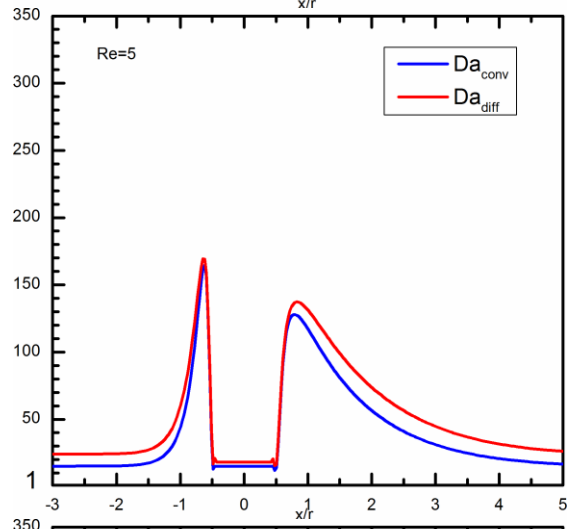
959

960

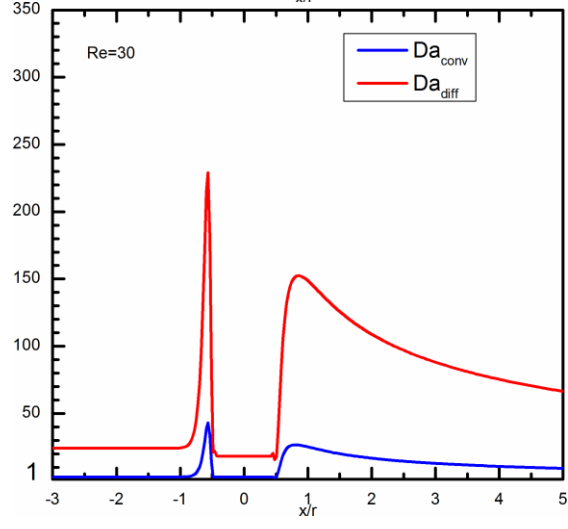
961



962



963



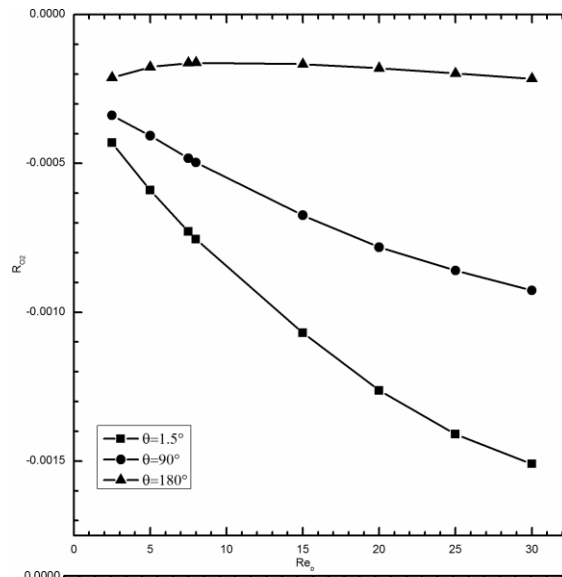
964

Figure 14. Distribution of convective and diffusive Da number along x at $y=0$

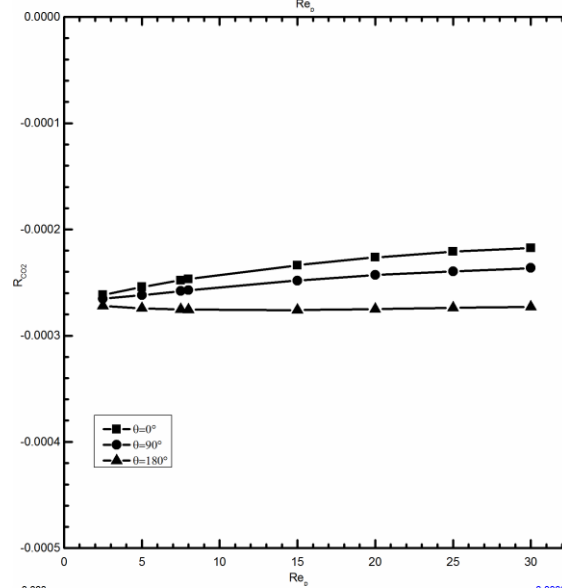
965

966

967



968

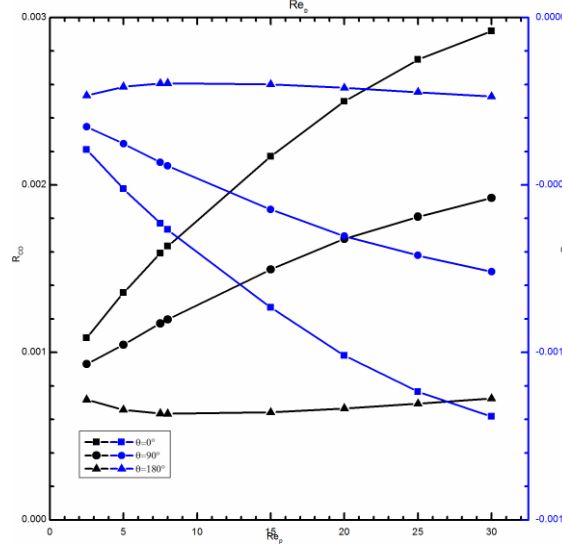


969
970

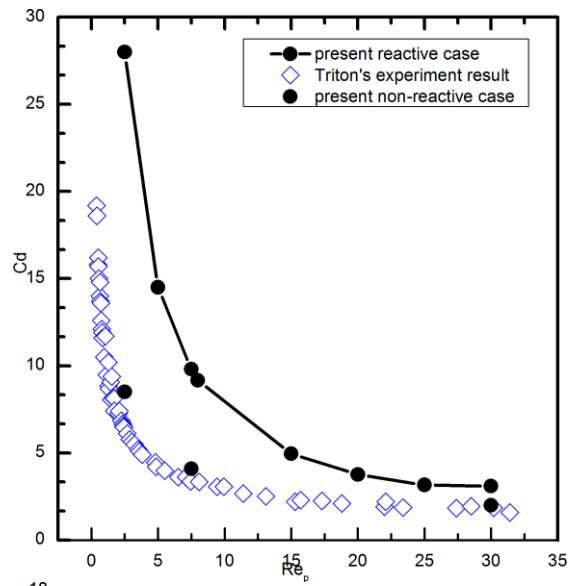
Figure 15. The local consumption or production rate of different species

971

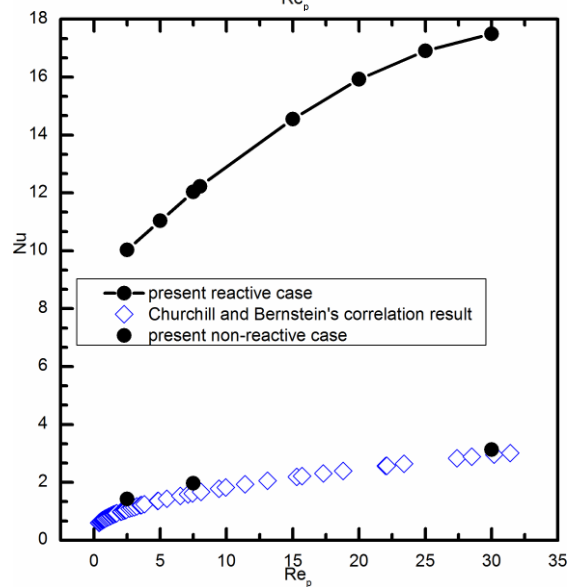
972



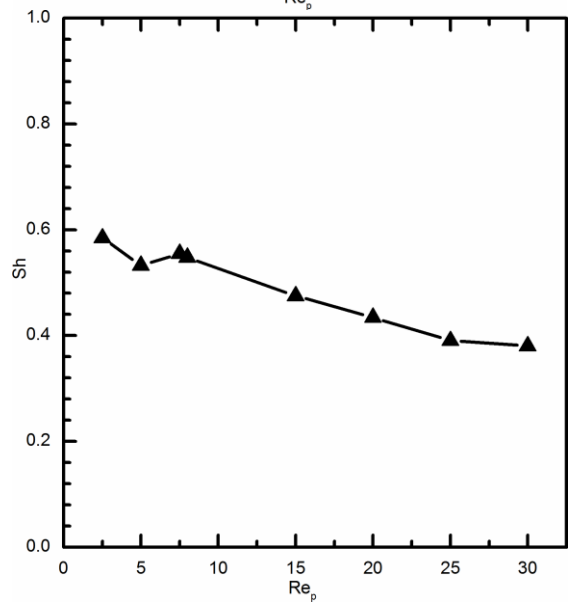
973



974

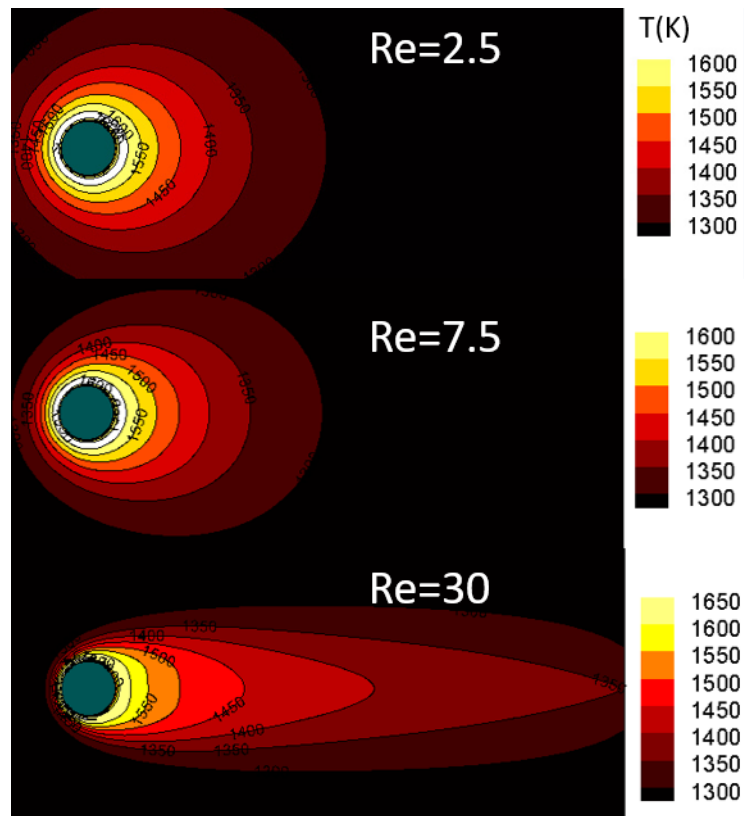


975



976

Figure 16. Evolution of C_d , Nu and Sh number with Reynolds number



977

978

Figure 17. Temperature contour under different Reynolds numbers

979

980

981

982

983

984

985

986

987

988

989

990

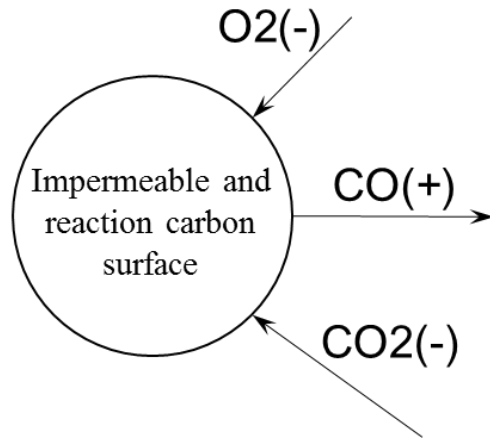
991

992

993

994

995



996

997

Figure 18. Schematic of a burning carbon surface

998

999

1000

1001

1002

1003

1004

1005

1006

1007

1008

1009

1010

1011

1012

1013

1014

1015

1016

1017

1018

1019

1020

1021

Table 1 Reaction kinetic constants

Chemical reaction		$K = B \exp(-E / RT)$		Reference
		B	$E(\text{J/mol})$	
R1	$2C + O_2 \rightarrow 2CO$	1.97×10^7	1.98×10^5	Zhang et al ⁴⁵
R2	$C + CO_2 \rightarrow 2CO$	1.291×10^5	1.91×10^5	Zhang et al ⁴⁵
R3	$2CO + O_2 \rightarrow 2CO_2$	2.24×10^{12}	1.6742×10^5	Nikrityuk et al ⁴⁶

1022

1023

1024

1025

1026

1027

1028

1029

1030

1031

1032

1033

1034

1035

1036

1037

1038

1039

1040

1041

1042

1043

1044

1045

1046

1047

1048

Table. 2 Averaged dynamic viscosity

Re	$\nu(g / (cm \cdot s))$		
	with reactions	without reactions	Inlet air
2.5	2.056784	1.960409	1.8255142
5	2.016095	--	
7.5	2.002146	1.918333	
8	1.999664	--	
15	1.974224	--	
20	1.963458	--	
25	1.957802	--	
30	1.956899	1.897289	

1049

1050

1051

1052

1053

1054

1055

1056

1057

1058

1059

1060

1061

1062

1063

1064

1065

1066

1067

1068

1069

1070

1071

1072

1073 **References**

- 1074 1. Nusselt W. Der verbrennungsvorgang in der kohlenstaubfeuerung. Zeitschrift des
1075 Vereins Deutsche Ingenieure. 1924;68:124-131.
- 1076 2. Burke S, Schumann T. Kinetics of a type of heterogeneous reactions the mechanism
1077 of combustion of pulverized fuel. Industrial & Engineering Chemistry.
1078 1931;23:406-417.
- 1079 3. Farazi S, Sadr M, Kang S, Schiemann M, Vorobiev N, Scherer V, Pitsch H. Resolved
1080 simulations of single char particle combustion in a laminar flow field. Fuel.
1081 2017;201:15-28.
- 1082 4. Peskin CS. Flow patterns around heart valves: A numerical method. Journal of
1083 Computational Physics. 1972;10:252-271.
- 1084 5. Peskin CS. The immersed boundary method. Acta Numerica. 2003;11:1-39.
- 1085 6. Haeri S, Shrimpton JS. On the application of immersed boundary, fictitious domain
1086 and body-conformal mesh methods to many particle multiphase flows. International
1087 Journal of Multiphase Flow. 2012;40:38-55.
- 1088 7. Mittal R, Iaccarino G. Immersed boundary methods. Annual Review of Fluid
1089 Mechanics. 2005;37:239-261.
- 1090 8. Sotiropoulos F, Yang X. Immersed boundary methods for simulating fluid–structure
1091 interaction. Progress in Aerospace Sciences. 2014;65:1-21.
- 1092 9. Fadlun EA, Verzicco R, Orlandi P, Mohd-Yusof J. Combined immersed-boundary
1093 finite-difference methods for three-dimensional complex flow simulations. Journal of
1094 Computational Physics. 2000;161:35-60.
- 1095 10. de Tullio MD, De Palma P, Iaccarino G, Pascazio G, Napolitano M. An immersed
1096 boundary method for compressible flows using local grid refinement. Journal of
1097 Computational Physics. 2007;225:2098-2117.

- 1098 11. Berthelsen PA, Faltinsen OM. A local directional ghost cell approach for
1099 incompressible viscous flow problems with irregular boundaries. *Journal of*
1100 *Computational Physics*. 2008;227:4354-4397.
- 1101 12. Ghias R, Mittal R, Dong H. A sharp interface immersed boundary method for
1102 compressible viscous flows. *Journal of Computational Physics*. 2007;225:528-553.
- 1103 13. Mittal R, Dong H, Bozkurttas M, Najjar FM, Vargas A, von Loebbecke A. A
1104 versatile sharp interface immersed boundary method for incompressible flows with
1105 complex boundaries. *Journal of Computational Physics*. 2008;227:4825-4852.
- 1106 14. Gilmanov A, Acharya S. A computational strategy for simulating heat transfer and
1107 flow past deformable objects. *International Journal of Heat and Mass Transfer*.
1108 2008;51:4415-4426.
- 1109 15. Gilmanov A, Sotiropoulos F. A hybrid cartesian/immersed boundary method for
1110 simulating flows with 3d, geometrically complex, moving bodies. *Journal of*
1111 *Computational Physics*. 2005;207:457-492.
- 1112 16. Shrivastava M, Agrawal A, Sharma A. A novel level set-based immersed-boundary
1113 method for cfd simulation of moving-boundary problems. *Numerical Heat Transfer,*
1114 *Part B: Fundamentals*. 2013;63:304-326.
- 1115 17. Kim J, Choi H. An immersed-boundary finite-volume method for simulation of heat
1116 transfer in complex geometries. *KSME International Journal*. 2004;18:1026-1035.
- 1117 18. Luo K, Zhuang Z, Fan J, Haugen NEL. A ghost-cell immersed boundary method for
1118 simulations of heat transfer in compressible flows under different boundary conditions.
1119 *International Journal of Heat and Mass Transfer*. 2016;92:708-717.
- 1120 19. Luo K, Mao C, Zhuang Z, Fan J, Haugen NEL. A ghost-cell immersed boundary
1121 method for the simulations of heat transfer in compressible flows under different
1122 boundary conditions part-ii: Complex geometries. *International Journal of Heat and*

1123 Mass Transfer. 2017;104:98-111.

1124 20. McGurn MT, Ruggirello KP, DesJardin PE. An eulerian–lagrangian moving
1125 immersed interface method for simulating burning solids. Journal of Computational
1126 Physics. 2013;241:364-387.

1127 21. Kedia KS, Safta C, Ray J, Najm HN, Ghoniem AF. A second-order coupled
1128 immersed boundary-samr construction for chemically reacting flow over a
1129 heat-conducting cartesian grid-conforming solid. Journal of Computational Physics.
1130 2014;272:408-428.

1131 22. Deen NG, Kuipers JAM. Direct numerical simulation of fluid flow accompanied by
1132 coupled mass and heat transfer in dense fluid–particle systems. Chemical Engineering
1133 Science. 2014;116:645-656.

1134 23. Dierich F, Richter A, Nikrityuk P. A fixed-grid model to track the interface and
1135 porosity of a chemically reacting moving char particle. Chemical Engineering Science.
1136 2018;175:296-305.

1137 24. <https://code.google.com/p/pencil-code/>.

1138 25. Babkovskaia N, Haugen NEL, Brandenburg A. A high-order public domain code
1139 for direct numerical simulations of turbulent combustion. Journal of Computational
1140 Physics. 2011;230:1-12.

1141 26. Wilke CR. A viscosity equation for gas mixtures. The Journal of Chemical Physics.
1142 1950;18:517-519.

1143 27. Coffee TP, Heimerl JM. Transport algorithms for premixed, laminar steady-state
1144 flames. Combustion and Flame. 1981;43:273-289.

1145 28. Mourits FM, Rummens FHA. A critical evaluation of lennard–jones and
1146 stockmayer potential parameters and of some correlation methods. Canadian Journal of
1147 Chemistry. 1977;55:3007-3020.

- 1148 29. Strohle J, Myhrvold T. An evaluation of detailed reaction mechanisms for hydrogen
1149 combustion under gas turbine conditions. *International Journal of Hydrogen Energy*.
1150 2007;32:125-135.
- 1151 30. <http://www.chemkin.com/>.
- 1152 31. Kee RJ, Coltrin ME, Glarborg P, *Chemically reacting flow: Theory and practice*,
1153 Wiley, Newark, NJ, 2003.
- 1154 32. Makino A, Namikiri T, Kimura K. Combustion rates of graphite rods in the forward
1155 stagnation field with high-temperature airflow. *Combustion and Flame*.
1156 2003;132:743-753.
- 1157 33. Yoo CS, Im HG. Characteristic boundary conditions for simulations of compressible
1158 reacting flows with multi-dimensional, viscous and reaction effects. *Combustion
1159 Theory and Modelling*. 2007;11:259-286.
- 1160 34. Walls JR, Strickland-Constable RF. Oxidation of carbon between 1000–2400 °C.
1161 *Carbon*. 1964;1:333-338.
- 1162 35. Yang RT, Steinberg M. A diffusion cell method for studying heterogeneous kinetics
1163 in the chemical reaction/diffusion controlled region. Kinetics of $C + CO_2 \rightarrow 2CO$ at
1164 1200–1600 °C. *Industrial & Engineering Chemistry*. 1977;16:235-242.
- 1165 36. Makino A, Araki N, Mihara Y. Combustion of artificial graphite in stagnation flow:
1166 Estimation of global kinetic parameters from experimental results. *Combustion and
1167 Flame*. 1994;96:261-274.
- 1168 37. Hees J, Zabrodiec D, Massmeyer A, Pielsticker S, Gövert B, Habermehl M,
1169 Hatzfeld O, Kneer R. Detailed analyzes of pulverized coal swirl flames in oxy-fuel
1170 atmospheres. *Combustion and Flame*. 2016;172:289-301.
- 1171 38. Richter A, Nikrityuk PA, Kestel M. Numerical investigation of a chemically
1172 reacting carbon particle moving in a hot O_2/CO_2 atmosphere. *Industrial & Engineering*

1173 Chemistry Research. 2013;52:5815-5824.

1174 39. Tritton DJ. Experiments on the flow past a circular cylinder at low reynolds
1175 numbers. Journal of Fluid Mechanics. 2006;6:547.

1176 40. Churchill B. A correlating equation for forced convection from gases and liquids to
1177 a circular cylinder in crossflow. Journal of heat transfer. 1977;99:7.

1178 41. Hecht ES, Shaddix CR, Lighty JS. Analysis of the errors associated with typical
1179 pulverized coal char combustion modeling assumptions for oxy-fuel combustion.
1180 Combustion and Flame. 2013;160:1499-1509.

1181 42. Gonzalo-Tirado C, Jiménez S. Detailed analysis of the co oxidation chemistry
1182 around a coal char particle under conventional and oxy-fuel combustion conditions.
1183 Combustion and Flame. 2015;162:478-485.

1184 43. Gonzalo-Tirado C, Jiménez S, Johansson R, Ballester J. Comparative study of four
1185 alternative models for co oxidation around a burning coal char particle. Combustion
1186 and Flame. 2014;161:1085-1095.

1187 44. Farazi S, Schiemann M, Vorobiev N, Scherer V, Pitsch H, Variable transport
1188 coefficients effects on the single-film model of char combustion, Combust. Meet.,
1189 Europe, 2017.

1190 45. Zhang L, Liu K, You C. Fictitious domain method for fully resolved reacting
1191 gas–solid flow simulation. Journal of Computational Physics. 2015;299:215-228.

1192 46. Nikrityuk PA, Gräbner M, Kestel M, Meyer B. Numerical study of the influence of
1193 heterogeneous kinetics on the carbon consumption by oxidation of a single coal particle.
1194 Fuel. 2013;114:88-98.

1195
1196
1197
1198

1199
1200
1201
1202
1203
1204
1205
1206
1207
1208
1209
1210
1211